

Studies of improved electron confinement in low density L-mode National Spherical Torus Experiment discharges

D. Stutman, M. Finkenthal, and K. Tritz
Johns Hopkins University, Baltimore, Maryland 21218

M. H. Redi, S. M. Kaye, M. G. Bell, R. E. Bell, B. P. LeBlanc, K. W. Hill, S. S. Medley,
 J. E. Menard, G. Rewoldt, and W. X. Wang
Princeton Plasma Physics Laboratory, Princeton, New Jersey 08543

E. J. Synakowski
Lawrence Livermore National Laboratory, Livermore, California 94550

F. Levinton
Nova Photonics, Princeton, New Jersey 08540

S. Kubota
University of California, Los Angeles, California 90095

C. Bourdelle
Association Euratom-CEA, Cadarache, France

W. Dorland
University of Maryland, College Park, Maryland 20742

The NSTX Team
Princeton Plasma Physics Laboratory, Princeton, New Jersey 08543

(Received 8 June 2006; accepted 23 August 2006; published online 29 September 2006)

Electron transport is rapid in most National Spherical Torus Experiment, M. Ono *et al.*, Nucl. Fusion **40**, 557 (2000) beam heated plasmas. A regime of improved electron confinement is nevertheless observed in low density L-mode (“low-confinement”) discharges heated by early beam injection. Experiments were performed in this regime to study the role of the current profile on thermal transport. Variations in the magnetic shear profile were produced by changing the current ramp rate and onset of neutral beam heating. An increased electron temperature gradient and local minimum in the electron thermal diffusivity were observed at early times in plasmas with the fastest current ramp and earliest beam injection. In addition, an increased ion temperature gradient associated with a region of reduced ion transport is observed at slightly larger radii. Ultrasoft x-ray measurements of double-tearing magnetohydrodynamic activity, together with current diffusion calculations, point to the existence of negative magnetic shear in the core of these plasmas. Discharges with slower current ramp and delayed beam onset, which are estimated to have more monotonic q -profiles, do not exhibit regions of reduced transport. The results are discussed in the light of the initial linear microstability assessment of these plasmas, which suggests that the growth rate of all instabilities, including microtearing modes, can be reduced by negative or low magnetic shear in the temperature gradient region. Several puzzles arising from the present experiments are also highlighted. © 2006 American Institute of Physics. [DOI: 10.1063/1.2355664]

I. INTRODUCTION

An understanding of ion thermal transport in tokamaks based on the interplay among ion gyroscale drift instabilities, $\mathbf{E} \times \mathbf{B}$ velocity shear, and magnetic shear has been theoretically and experimentally consolidated in recent years.^{1–4} An overview of the role of sheared $\mathbf{E} \times \mathbf{B}$ flow in turbulence suppression can be found in Ref. 2, while a recent overview of the role of negative magnetic shear in the formation of transport barriers can be found in Ref. 3. The control and sustainment of such barriers is discussed in Ref. 4.

Developing a similar understanding of electron thermal transport remains, however, a major challenge for all toroidal confinement devices.^{1–3} One reason for this is that, starting from electron gyroscale instabilities, highly nonlinear pro-

cesses need to be invoked in order to explain the electron heat diffusivity observed in experiments.

Due to its low aspect ratio, high beta, and low toroidal field, transport in the spherical torus (ST) was predicted to be different from that in the large-aspect-ratio tokamak.⁵ Early linear microstability calculations indicated that the large $\mathbf{E} \times \mathbf{B}$ shear achievable at low field should facilitate suppression of ion anomalous transport.⁶ This prediction was supported by initial observations of ion thermal and particle transport near neoclassical levels in the National Spherical Torus Experiment (NSTX, Ref. 7) at Princeton and in the Mega-Ampère Spherical Tokamak (MAST) at Culham.^{8–12} On the other hand, the calculations also suggested the possibility that at high beta, magnetic instabilities such as mi-

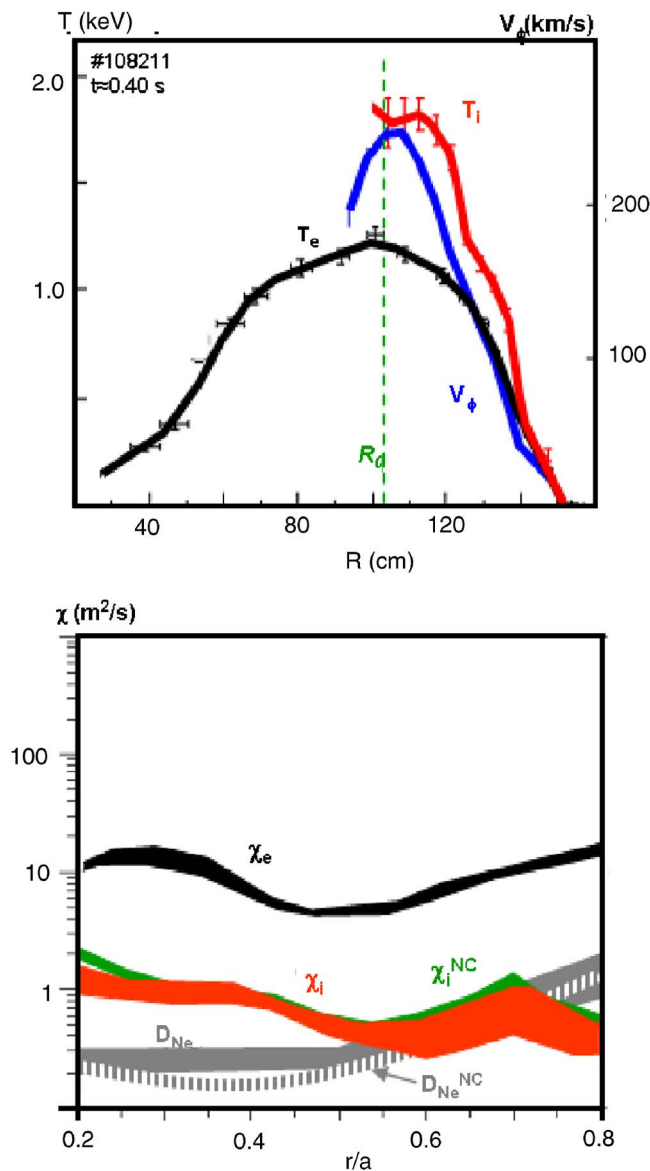


FIG. 1. Plasma profiles and thermal diffusivities in intermediate density L-mode (1 MA, 4.5 kG, $P_{\text{beam}}=1.8$ MW, $\beta \approx 15\%$). Also shown the neoclassical diffusivity χ_i^{NC} computed by the NCLASS code and the measured and NCLASS computed neon diffusivity (Ref. 9). The band of values indicates the variability in the TRANSP diffusivity calculation over a 20 ms interval.

crotearing modes,^{6,13} could preferentially increase the electron thermal losses and indeed, the electron thermal transport rates reported thus far, exceed the ion ones for most discharge scenarios.^{8–12}

The picture of transport dominated by electrons in neutral beam heated NSTX plasmas is illustrated for intermediate density and beta L-mode (“low-confinement”) discharges ($\langle n_e \rangle \approx 4 \times 10^{13} \text{ cm}^{-3}$, $P_{\text{beam}}=1.8$ MW, $\beta \approx 15\%$ at $t \approx 0.4$ s), in Fig. 1. As seen, the core ion temperature T_i exceeds the electron temperature T_e by up to 50%, although the beams preferentially heat the electrons relative to the ions by a 2:1 ratio.⁸ This is reflected in the electron thermal diffusivity, χ_e , being in the ≈ 5 – $15 \text{ m}^2/\text{s}$ range throughout the plasma and significantly exceeding the ion thermal diffusivity χ_i . (The comparison is restricted to the radial region $0.2 < r/a < 0.8$, where the uncertainty in the inferred transport coefficients is

low.⁸) On the other hand, over a broad plasma region the ion diffusivity falls in the range of the neoclassical diffusivity $\chi_i^{\text{NC}} \leq 1 \text{ m}^2/\text{s}$, as computed by the NCLASS code.¹⁴ High plasma rotation velocities also point to momentum diffusivity below $\approx 1 \text{ m}^2/\text{s}$.⁸ Although the NCLASS calculations do not take into account possible finite orbit enhancements to the neoclassical diffusivity, by up to a factor of ≈ 2 ,¹⁵ this suggests that anomalous ion transport must be suppressed in these strongly rotating plasmas. An additional indication for the suppression of long-wavelength turbulence comes from perturbative impurity transport measurements, which show that the diffusivity of injected neon is comparable to the NCLASS neoclassical prediction of $< 1 \text{ m}^2/\text{s}$. Such low particle diffusivity suggests very low growth rates for long-wavelength instabilities, as discussed in Ref. 9. Comparable trends are observed in high power and density NSTX H-modes (“high-confinement”)⁸ and in MAST discharges.^{10,11} This transport ordering is in contrast with the typical large-aspect-ratio tokamak picture, where in L-modes the ion transport is well above neoclassical and χ_e is comparable to χ_i .

The question therefore arises as to whether the rapid electron transport is intrinsic to the ST or if there are ways to reduce it. A tool often used successfully to reduce electron transport in large-aspect-ratio tokamaks is creating a region of negative magnetic shear.^{1,3} A systematic study of the effects of the magnetic shear on thermal transport has therefore been carried out at NSTX. The present paper reports the first experimental results from this study.

II. EXPERIMENTS ON ELECTRON TRANSPORT REDUCTION

In order to study the effects of changes in the magnetic shear, plasmas are compared with different magnetic shear profiles, but with other parameters potentially important for thermal transport, as similar as possible. Such critical parameters include the $\mathbf{E} \times \mathbf{B}$ shear (largely determined by the toroidal rotation profile in NSTX L-modes⁹), β , the density profile, and the T_i/T_e ratio.¹ In addition, the discharges were designed to be as free as possible of magnetohydrodynamic (MHD) activity, such as low- n tearing modes or internal reconnection events, for a transport relevant comparison to be made.

Low density ($\langle n_e \rangle \approx 2 \times 10^{13} \text{ cm}^{-3}$), neutral beam heated L-mode discharges were chosen for this study, because the large power input per particle enabled better heating of the core electrons, slowing down of the current diffusion and eventual reversal of the q -profile. In order to vary the magnetic shear, the plasma current ramp-rate and beam timing were varied, while keeping the beam power fixed at 2 MW. Double-null diverted discharges having 1 MA current, 0.45 T toroidal field, elongation $\kappa \approx 1.8$ – 2 , and average triangularity $\delta \approx 0.6$ – 0.7 were used as a baseline. Experiments of internal barrier formation in low density L-mode discharges have also been performed at MAST.¹⁶

In Fig. 2 the time histories obtained at low density with fast current ramp and early beam injection (solid lines, shot #112989, 6.5 MA/s, $t_{\text{beam,on}} \approx 0.05$ s) are compared with

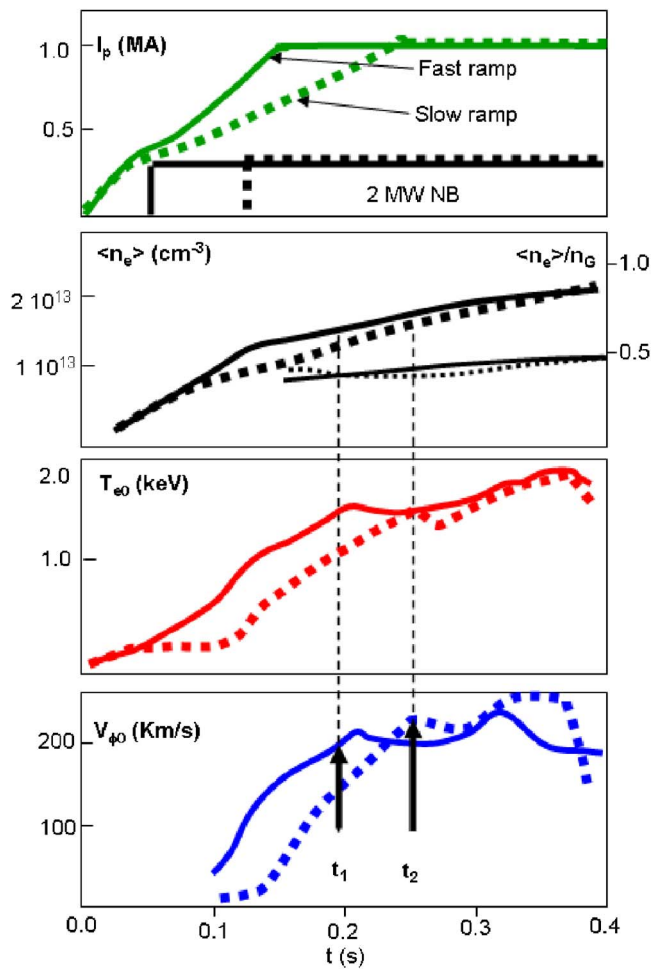


FIG. 2. Time histories of plasma current, line averaged electron density, central electron temperature, and central toroidal velocity, for fast ramp rate (shot #112989, solid lines) and slow ramp rate (shot #112996, dotted lines) low density L-mode discharges (1 MA, 0.45 T). The density is also shown as a fraction of the Greenwald limit n_G (thinner lines).

those obtained with slow current ramp and late beam injection (dotted lines, shot #112996, 4 MA/s, $t_{\text{beam,on}} \approx 0.12$ s). The time histories of line-averaged density are comparable, while in both cases T_{e0} increases to ≈ 1.5 keV after 0.12–0.15 s of beam heating. The sudden change in the T_{e0} trace occurring in both plasmas after the initial rise (near $t \approx 0.22$ s in the fast ramp case and $t \approx 0.26$ s in the slow ramp case) is associated with larger reconnection, or transport events. Before these times, the ultrasoft x-ray (USXR) data indicate that in both cases the plasma core is free from large reconnection events, although a small off-axis reconnection is identified in the fast ramp shot #112989 around 0.182 s. In addition, shortly before the large reconnection at $t \approx 0.22$ s in the same plasma, a 2/1 mode is indicated by the USXR and magnetic data, localized inside $r/a \approx 0.4$.

The traces of the central toroidal velocities are also shown in Fig. 2. As seen, before $t \approx 0.22$ s in the fast ramp case and before $t \approx 0.26$ s in the slow ramp case, the rotation velocities become comparable. In the following discussion, the points $t_1 \approx 0.19$ s in the fast ramp case and $t_2 \approx 0.25$ s in the slow ramp case will be used as times of transport comparison, since they satisfy both the requirement for similar

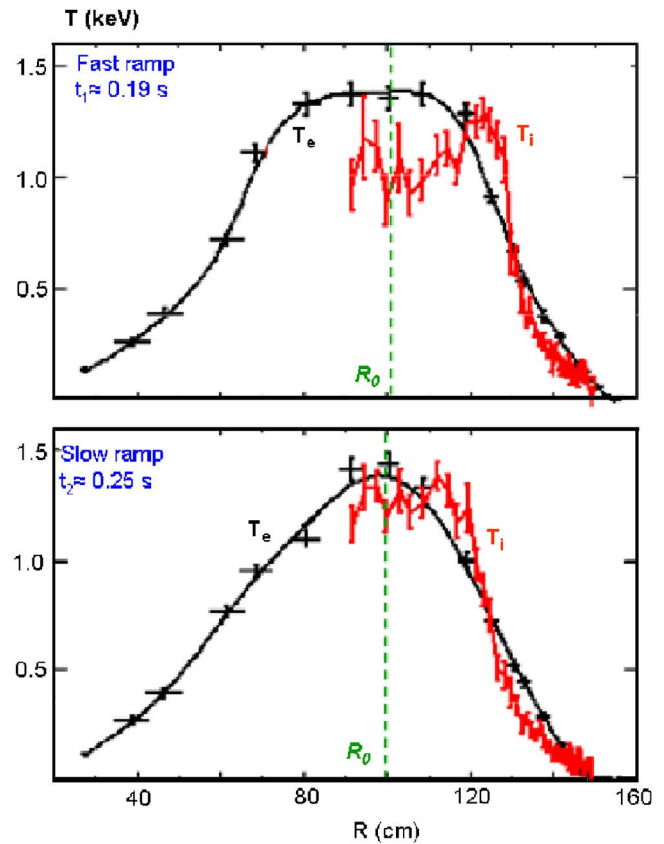


FIG. 3. Electron and ion temperature profiles in the fast and slow ramp cases. The solid lines represent spline fits to the experimental points. Also shown is the radius of the magnetic axis computed by TRANSP assuming magnetic diffusion.

rotation and for absence of low- n MHD activity. The Mirnov coil data at t_1 and t_2 show only high-frequency [≈ 80 –160 kHz, toroidal Alfvén eigenmodes (TAE) range], high- n (3–5 in #112989 and 2–4 in #112996) MHD activity in both discharges. The spectrum of deuterium beam energetic ions measured by the neutral particle analyzer on NSTX does not show any MHD-induced ion depletion, due to either anomalous MHD-induced effects,¹⁷ or classical charge exchange emissivity profile effects.¹⁸ Good agreement between the measured neutron rate and that calculated by the TRANSP code¹⁹ also supports the absence of significant energetic ion loss.

The elongation κ , and plasma volume V_p , are relatively similar for the two discharges. At the times of interest, t_1 and t_2 , $\kappa_1 = 1.75$, $\kappa_2 = 1.88$, $V_{p1} = 11.4$ m³, $V_{p2} = 11.0$ m³. The triangularity δ , differs by about 15%; i.e., $\delta_1 = 0.62$ and $\delta_2 = 0.73$.

The experimental electron and ion temperature profiles at the times of interest are shown in Fig. 3. Although the central values are comparable, the fast ramp case has steeper gradients in both the electron and ion profiles around mid-radius. An interesting observation is the flattening of the T_e profile between $R \approx 80$ cm and $R \approx 120$ cm ($r/a \leq 0.2$), despite the absence of MHD reconnections. Within the uncertainty illustrated by the error bars in Fig. 3, the central T_i profile appears hollow in the fast ramp case.

While the T_i profile is measured with about 1 cm spac-

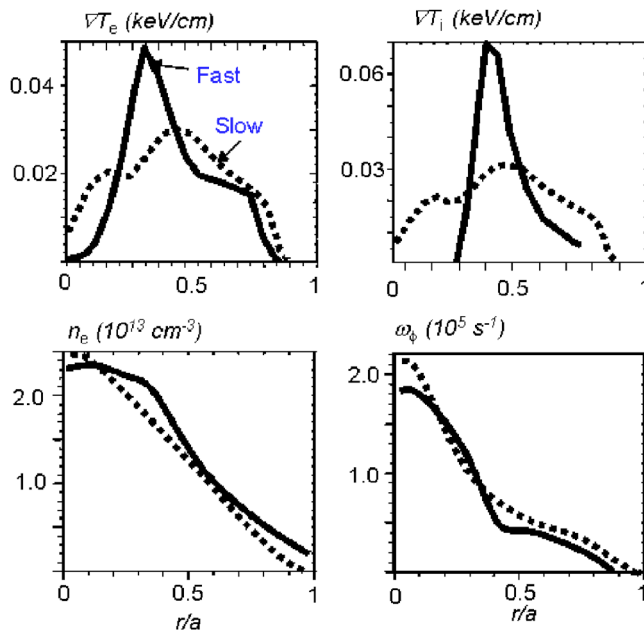


FIG. 4. TRANSP computed gradients of electron and ion temperature in the fast and slow ramp cases. Also shown are the electron density and toroidal rotation profiles.

ing, the separation of the points in the T_e profile is ≥ 6 cm in the core. It is thus possible that in the fast ramp case the T_e gradient is in reality even stronger than is indicated by the spline fit to the Thomson scattering points in Fig. 3. This is suggested by the profiles of the temperature sensitive ($E > 1.4$ keV) USXR emission obtained with a vertically viewing diode array.

The spline fit of the Thomson scattering data in Fig. 3 will nevertheless be used as a basis for the present comparisons. Figure 4 compares the thermal gradients computed by the TRANSP code, as well as the flux surface mapped electron density and toroidal rotation profiles. While the electron and ion temperature gradients are about twice as large in the fast ramp case, the rotation profiles are relatively similar in the two cases, at the two respective times. Both profiles show a shallow gradient going from the edge to $r/a \approx 0.4$ (with a plateau in the fast ramp case) followed by a rapid increase to high rotation in the inner core region. The appearance of the rotation plateau in the fast ramp case seems associated with the growth of the 2/1 mode mentioned above. The electron density profile also shows a region of increased gradient in the fast ramp case. The average toroidal beta is $\approx 8\%$ in both cases.

III. INDICATIONS FOR MAGNETIC SHEAR REVERSAL WITH FAST RAMP

The motional Stark effect (MSE) diagnostic for the magnetic field pitch angle was not available in these experiments. To assess how the magnetic shear changed between the fast and slow ramp cases, MHD information from USXR and magnetic data, as well as magnetic diffusion calculations were used. The layout of the NSTX USXR system is sketched in Fig. 5, while a detailed description can be found in Ref. 20 and references therein. Its main characteristic is

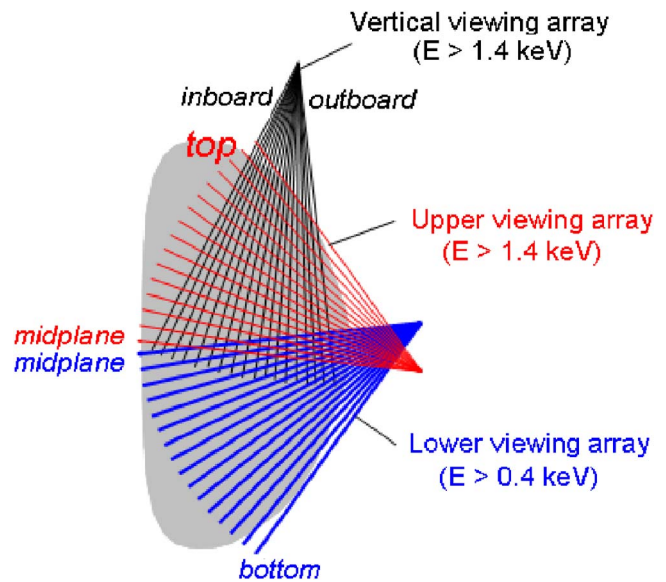


FIG. 5. Layout of the NSTX ultrasoft x-ray system (see Ref. 20). Also shown are the array and chord labeling used throughout the paper.

the capability for simultaneous imaging in multiple energy ranges. Due to the dependence of the plasma emissivity on the electron temperature, selective imaging of MHD activity in the core or outer plasma regions, as well as fast “two-color” measurement of electron temperature perturbations is possible.²⁰

The analysis of ultrasoft x-ray and magnetic data points to a broad region of magnetic shear reversal in the fast ramp, early injection discharges, for which one finds several indications. First, both at early and late times in these shots, the high energy, T_e sensitive USXR profiles display small, off-axis sawtooth-like crashes, in which only the outer plasma emission is involved. Similar MHD behavior was later seen in plasmas in which the MSE diagnostic was operating, and indicated negative shear.

Second, at later times, two coherent 1/1 modes at distinct radii, indicative of the existence of two $q=1$ surfaces in the plasma, were observed to be associated with these crashes. Intensity plots of the USXR fluctuation amplitude measured with the upper and lower viewing horizontal arrays are shown in Fig. 6(a). The high-frequency noise and the dc component are subtracted using Singular Value Decomposition (SVD) and retaining only the first few pairs of singular values.²¹ The fluctuation amplitudes in each array are normalized to the central chord dc component. The upper viewing array was filtered with $100 \mu\text{m}$ Be for $E > 1.4$ keV spectral response, while the lower viewing array with $5 \mu\text{m}$ Be for $E > 0.4$ keV response. The different energy response confers the two arrays different sensitivity to temperature perturbations.²⁰ The spatial profile of the power spectrum at the mode frequency is also plotted as a function of chord number on the right of the intensity plots in Fig. 6(a). The power spectrum is obtained by Fourier analysis of a 1 ms time block, centered at 377.4 ms. The profile is also normalized to the central chord dc power. The normalized amplitudes in the $E > 0.4$ keV spectrum are lower than in the

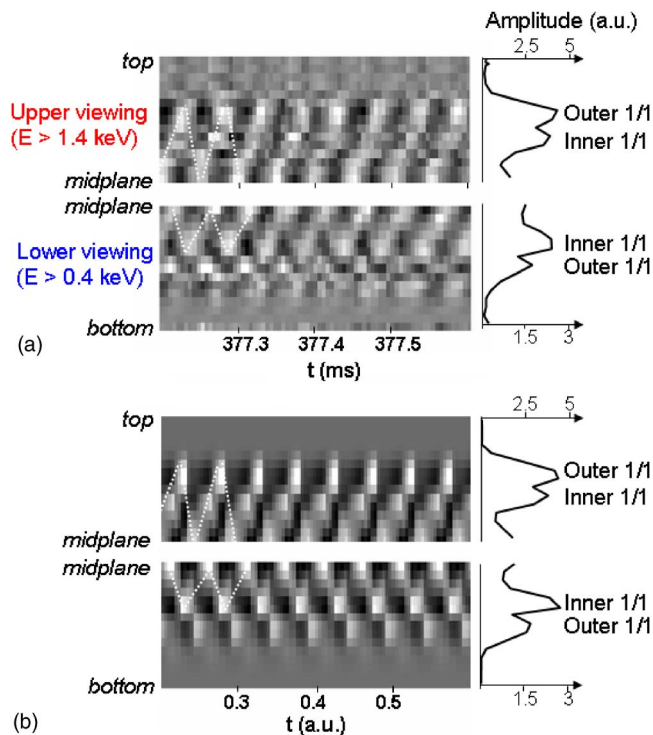


FIG. 6. (a) Intensity plots of fluctuations measured by the horizontal arrays in Fig. 6 in the fast ramp discharge. Two 1/1 modes are measured at different radii with different amplitudes, due to the different spectral response. The mode amplitude is shown on the right. (b) Similar plots, but for two simulated “island-like” perturbations, rotating on two distinct $m=1/n=1$ trajectories in shot #112989, on the magnetic flux surfaces computed at $t=377$ ms. The characteristic half-helix trajectories of 1/1 perturbations are sketched by dashed white lines. The fit to the power spectra in the two energy ranges obtains with the inner mode carrying predominantly a $n_e \times n_z$ perturbation and the outer mode predominantly a T_e perturbation.

$E > 1.4$ keV one, due to the stronger dc component in the low energy USXR emission.

A complex oscillation pattern with a fundamental frequency $f \approx 20$ kHz is seen in Fig. 6(a). The magnetic fluctuation data in the same time window show only $n=1$ activity, at the same frequency. The USXR analysis indicates, however, that more than one mode is present. First, the inner perturbation in the lower viewing array shows the characteristic “half-helix” trajectory of a 1/1 mode (the “half-helix” arises because only the lower plasma half is imaged). That this is a distinct internal mode and not part of a single outer mode of higher- m , it is also evident from the accompanying power spectrum profile. The profile exhibits two peaks, with the inner one having highest amplitude. Since, due to line integration, the maximum amplitude in the USXR fluctuation arises approximately in the cord tangent to the perturbation, the fact that the inner peak has higher amplitude indicates that a distinct inner mode exists inside the outer one.

The second, outer mode is locked in frequency and phase with this inner 1/1 mode. The frequency lock is consistent with the broad rotation profile in this shot at $t \approx 0.377$ s, in which the angular rotation frequencies at the major radii of the inner and of the outer modes ($R \approx 110$ cm and $R \approx 123$ cm at the outboard side, respectively) are nearly the same, about 20 kHz. As seen in Fig.

6(a), this outer mode is more evident in the higher energy image, where its associated spectral peak exceeds that of the inner 1/1 mode. Due to the fainter signals at higher energy and to the superposition of the two modes, it is more difficult in this case to directly assess a poloidal mode number from the trajectory of the USXR perturbation. However, since the magnetic data indicates that only $n=1$ perturbations are present at this time and since the 2/1 and higher rational surfaces can be estimated to be too far out in this plasma to explain the outer mode, this second mode is with high likelihood another 1/1 mode.

To verify this assertion in more detail a numerical simulation was carried out of how two 1/1 modes, rotating at equal frequency and locked in phase as in Fig. 6(a), would look in the USXR data. In this simulation we assumed that two island-like perturbations, conformal with the magnetic flux surfaces, follow the $q=1$ field line trajectory computed by the magnetic reconstruction. Since only one $q=1$ surface obtains from the magnetic data, we simulated two distinct 1/1 trajectories by compressing and respectively expanding the (R, Z) coordinates of the 1/1 field line by a multiplicative factor of the order of the unity. Each perturbation was assigned a central radius, a radial and poloidal extent and a T_e and/or $n_e \times n_z$ perturbation amplitude. A mild emissivity gradient at the island boundary was also included. The emissivity perturbations were then superimposed on a background emissivity, computed using the equilibrium electron density and temperature measured by Thomson scattering, and the carbon density measured by charge exchange spectroscopy. Lastly, the island parameters were fit by matching the experimental and computed radial profiles of the power spectra at the mode frequency, for both $E > 0.4$ keV and $E > 1.4$ keV.

The results of these “two-color” USXR simulations are shown in Fig. 6(b). The best fit is obtained for an outer 1/1 mode having several cm radial extent and carrying predominantly a T_e perturbation of $\approx 20\%$ amplitude and an inner 1/1 mode having comparable radial extent but carrying a predominantly $n_e \times n_z$ perturbation, of similar amplitude. The different temperature and density perturbations associated with the two modes are reflected in the different spectral power profiles obtained in the two energy ranges. Qualitative agreement is also obtained between the SVD filtered images of the experimental [Fig. 6(a)] and simulated [Fig. 6(b)] USXR fluctuation patterns.

In conclusion, the USXR data indicate the existence of two $m=1/n=1$ perturbations at later times in the fast ramp case, suggesting the existence of two $q=1$ surfaces and substantial shear reversal. Since the reversal survived several off-axis reconnections, one can surmise that at earlier times the q -profile must have also been substantially reversed. The slow ramp discharge on the other hand, does not exhibit the USXR signatures for substantial shear reversal.

The interpretation of the USXR perturbation pattern in Fig. 6(a) as indicative of strong shear reversal was later confirmed when the MSE diagnostic became operational at NSTX. An oscillation pattern identical to that in Fig. 6(a) was consistently observed around $t \approx 0.35$ s in low density L-mode discharges in which the q -profile had $q \approx 2$ on axis and $q \approx 1$ at $r/a \approx 0.5$. Nevertheless, due to coil system

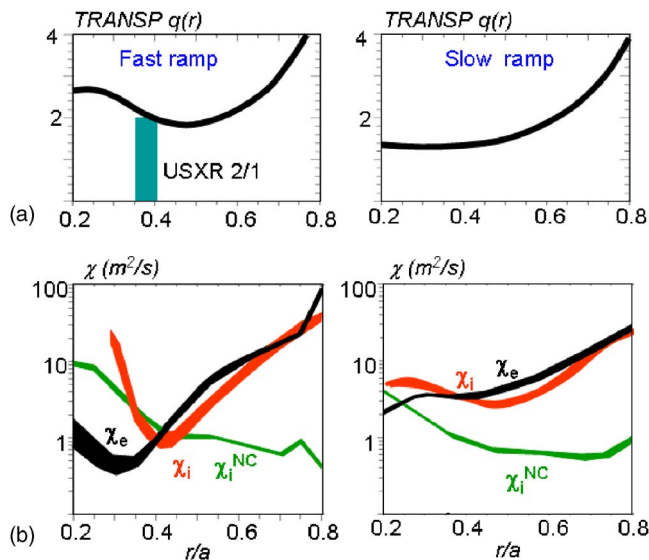


FIG. 7. (a) q -profiles computed by TRANSP for the fast and slow ramp cases assuming magnetic diffusion and the Sauter resistivity model.¹² The radial location of the 2/1 mode measured by the USXR system corroborates the radius of the $q=2$ surface computed by TRANSP. (b) Electron and ion thermal diffusivities computed by TRANSP for the two cases. Also shown, the NCLASS neoclassical prediction for the ion diffusivity. As above, the bands represent the 20 ms variability in the TRANSP calculation.

changes, the fast ramp shot #112989 could not be reproduced after the MSE diagnostic became operational. TRANSP modeling was therefore used to assess the differences in the current distribution between the fast and slow ramp discharges. Nevertheless, since the USXR assessment of the q -profile is done at late times, there may be some uncertainty in the evolution of the TRANSP computed q -profiles, early in the discharge.

The TRANSP simulations with different mapping options for the measured plasma profiles (e.g., using either only the outboard Thomson scattering profiles, or the entire in/out profiles) consistently indicate a broad region of negative shear throughout the fast ramp discharge, in agreement with the assessment from the USXR data. The slow ramp case on the other hand, has flat or only slightly reversed q -profile. The safety factor profiles computed by TRANSP at time t_1 in the fast ramp case and time t_2 in the slow case, are plotted in Fig. 7(a).

IV. TRANSPORT CHANGES WITH Q-PROFILE

The results of the power balance analysis of the two discharges are shown in Fig. 7(b) and indicate that large differences in transport are associated with the different q -profiles. In the fast ramp case a strong reduction in χ_e is seen in the region $r/a \approx 0.3-0.45$, indicative of an electron internal transport barrier (ITB). As above mentioned, the USXR data suggest that the electron gradient might be larger and therefore the ITB even more pronounced. There is also a large reduction in χ_i toward neoclassical values for $r/a=0.4-0.5$, indicating an ion ITB as well. In the slow ramp case on the other hand, χ_e increases rather monotonically from the center outward, while χ_i stays above several

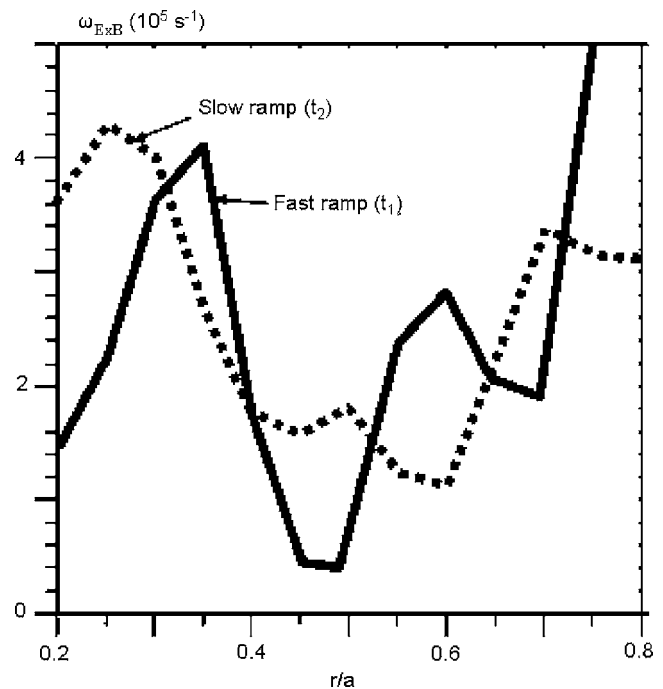


FIG. 8. $\mathbf{E} \times \mathbf{B}$ shearing rates computed by NCLASS for the slow and fast ramp cases at the times used in the transport comparison.

m^2/s at all radii. The global confinement times also differ, with $\tau_E \approx 70$ ms at t_1 in the fast ramp case and $\tau_E \approx 40$ ms at t_2 in the slow ramp case.

The local $\mathbf{E} \times \mathbf{B}$ shearing rates computed by TRANSP based on the Hahm-Burrell formulation²² and using outboard plasma profiles at times t_1 and t_2 in the two discharges, are plotted in Fig. 8. Primarily as a consequence of the similar rotation profiles, the two plasmas have relatively similar (and large) $\mathbf{E} \times \mathbf{B}$ shearing rates over much of the radius. Preliminary calculations with the GTC-NEO neoclassical transport code, which includes finite orbit width effects,²³ give a larger shearing rate at the ion ITB location than NCLASS. These calculations do not yet include the impurity species however.

Accepting the TRANSP and USXR indications for shear reversal with the fast ramp, the above results indicate a positive correlation between improved electron confinement and strong (less than ≈ -1.0) negative magnetic shear s , in the low density NSTX L-modes. Indeed, the location of minimum χ_e in the fast ramp case approximately coincides with the region of large negative shear ($s < -1.5$). This trend continues also at later times. The slow ramp plasma with flat, or only weakly reversed q -profile on the other hand, does not exhibit the broad electron barrier.

The magnetic shear appears to also have a strong impact on ion transport. Thus, other conditions being comparable, the slow ramp shot does not exhibit the pronounced ion ITB seen in the fast ramp case around $r/a=0.4-0.5$. In addition, as above mentioned, the ion ITB consistently appears to be located at a larger radius than the electron one. Assuming the TRANSP q -profile evolution, the electron barrier is situated in the region of large negative shear, while the ion barrier is rather in the region of low negative shear, near q_{\min} .

The above observations are further supported by data

TABLE I. GS2 predicted growth rates for electrostatic and electromagnetic instabilities in the fast and slow ramp discharges, in units of 10^5 s^{-1} . The magnetic shear s , used in the calculations, is also shown.

	Fast ramp #112989, $t_1=0.19 \text{ s}$			Slow ramp #112996, $t_2=0.25 \text{ s}$		
	$r/a=0.35$	$r/a=0.45$	$r/a=0.6$	$r/a=0.35$	$r/a=0.45$	$r/a=0.6$
ITG/TEM	Stable	Stable	1.8	Stable	0.6	1.4
μ -tearing ($k_{\theta}\rho_i < 1$)	0.2	Stable	Stable	1.0	Stable	Stable
ETG	Stable	Stable	8.0	Stable	5.5	8.0
s	-1.7	-0.7	2.3	0.03	0.7	2.3

from fast ramp shots, but in which the beam was delayed in comparison with #112989, in order to allow more rapid current penetration and thus a narrower region of shear reversal. In these cases, χ_e is still reduced, but at a smaller radius, which is again coincident with a negative shear region calculated by TRANSP. The ion barrier, although less pronounced, is also at a smaller radius in these plasmas. As suggested by the vertical array USXR data, the slow ramp shot #112996 might also represent an extreme case of such a situation, with a narrow region of negative shear and improved electron confinement close to the axis. This might eventually explain the χ_e decrease seen at $r/a < 0.25$ in the right panel of Fig. 7(b).

V. MICROSTABILITY ASSESSMENT

To guide the search for the possible mechanisms of anomalous electron transport in NSTX, linear gyrokinetic microstability calculations for these plasmas were performed with the GS2 code.²⁴ Although these calculations are local (“flux-tube” approximation), do not account for $\mathbf{E} \times \mathbf{B}$ shear, and are restricted in their applicability at low magnetic shear, they can indicate where in the $k_{\theta}\rho_i$ spectrum a strong linear drive (growth rate) for instability exists for the experimental plasma gradients. The results²⁵ are summarized in Table I for radii corresponding to the electron and ion ITB in the fast ramp case ($r/a \approx 0.35$ and $r/a \approx 0.45$, respectively), as well as for an outer radius $r/a \approx 0.6$, where the electron and ion transport is rapid in both discharges.

There are a few observations that can be made. The first is that low or negative magnetic shear is predicted to have a stabilizing effect on all electrostatic instabilities. For instance, at $r/a \approx 0.45$, the longer-wavelength ion temperature gradient and trapped electron mode (ITG/TEM) instabilities are stabilized due to shear changing from $+0.7$ in the slow ramp case, to -0.7 in the fast ramp case. This occurs in spite of the doubled T_i gradient, which is the drive for the instability, in the faster current ramp case (Fig. 4).

In addition, the short-wavelength electron temperature gradient (ETG) instability drive is completely suppressed at $r/a \approx 0.45$ and at $r/a \approx 0.35$ by negative magnetic shear in the fast ramp case, despite the increased T_e gradient. At reduced T_e gradient $s \approx 0$ has also a stabilizing effect, as indicated by the absence of ETG drive in the slow ramp case at $r/a \approx 0.35$. This trend is more clearly illustrated in Fig. 9, with GS2 results of a numerical scan of the magnetic shear at $r/a \approx 0.4$ in an intermediate density L-mode discharge. All

other parameters were kept fixed in these GS2 calculations; no attempt was made to self-consistently recalculate the equilibrium for each value of magnetic shear. In particular, the T_e gradient was kept fixed at the experimental value of $\approx 0.027 \text{ keV/cm}$ in this scan, which is comparable to the gradient at mid-radius in the slow ramp case (Fig. 4). As seen, increasingly negative shear suppresses the ETG growth rates, with zero growth rates at $s \approx -0.5$.

Another interesting aspect is the prediction of significant drive for long-wavelength microtearing modes at $r/a \approx 0.35$ in the slow ramp case. These modes are electromagnetic instabilities driven by the electron temperature gradient and have associated radial magnetic field perturbations.^{13,25,26} Such perturbations could, in principle, drive rapid transport predominantly in the electron channel,^{6,13} as is observed for instance in the high density NSTX H-mode^{8,25} and the intermediate density L-mode in Fig. 1. Recent nonlinear microstability calculations for MAST discharges also indicate a significant role for microtearing modes.¹⁵

In the central region ($r/a < 0.25$) of the slow ramp plasma no instability drive is computed by GS2, while the inferred electron transport is still relatively rapid. This may

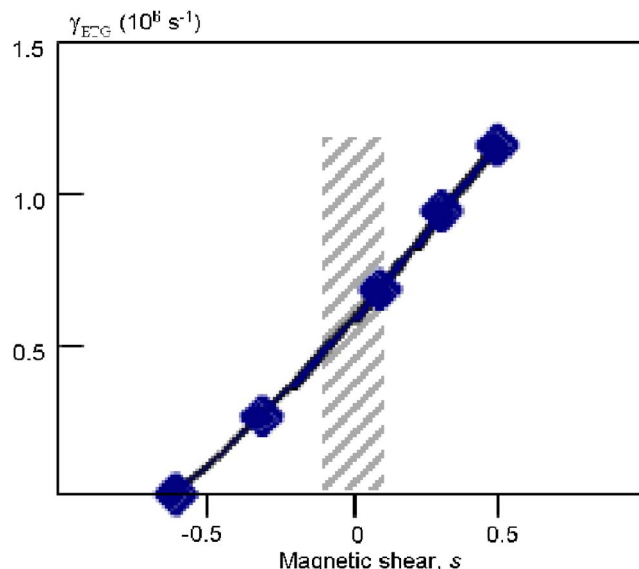


FIG. 9. Growth rates of high $k_{\theta}\rho_i$ (≈ 35) ETG modes calculated by GS2 at $r/a=0.4$, as a function of magnetic shear (shot #108213, $t \approx 0.29 \text{ s}$). In the shaded area the ballooning approximation used in the GS2 calculation is less accurate.

suggest non-local effects in NSTX transport.²⁷ Global transport codes are under development to address this possibility.²⁸ Three-dimensional MHD turbulence simulations also show that nonlocal effects may be involved in tokamak transport.²⁹

Finally, at $r/a \approx 0.6$, the linear calculations predict in both plasmas large growth rates for electrostatic instabilities of all wavelengths. This would appear consistent with the rapid electron and ion transport inferred for both discharges at this radius. However, as shown in Fig. 8, due to the strong toroidal rotation, the estimated local $\mathbf{E} \times \mathbf{B}$ velocity shearing rates are also rather high throughout most of the plasma, in both discharges. While our experimental results indicate that magnetic shear has a clear effect on transport in these plasmas, it is difficult to assess the role of the $\mathbf{E} \times \mathbf{B}$ velocity shear through comparisons with the linear microstability predictions. Nonlinear calculations incorporating $\mathbf{E} \times \mathbf{B}$ shear indicate that a large variability may exist in the level of velocity shear needed to suppress turbulence.³⁰ In our case, for instance, in the slow ramp discharge χ_i exceeds the neoclassical levels by a substantial factor in the region $r/a \approx 0.45$, although the $\mathbf{E} \times \mathbf{B}$ shearing rate is a few times larger than the predicted ITG-TEM growth rates. It is therefore quite possible that the transport changes observed in these experiments reflect the interplay between the reduction of instability drive by negative magnetic shear and turbulence suppression by $\mathbf{E} \times \mathbf{B}$ shear. Nonlinear, full-torus gyrokinetic simulations with the GYRO code³⁰ are underway to assess the role of $\mathbf{E} \times \mathbf{B}$ shear in these plasmas.

As concerns fluctuation data, density correlation length measurements performed in these plasmas using microwave reflectometry show correlation lengths of several cm in the core of both fast and slow ramp discharges. The fast ramp case has somewhat shorter correlation lengths and smaller density fluctuation amplitude, early in time. The interpretation of the results in terms of turbulent fluctuations is, however, complicated by the influence of high-frequency (TAE range) MHD activity.

VI. QUESTIONS FROM THE EXPERIMENTS

While the above experiments indicate a definite correlation between transport and q -profile changes on NSTX, they also bring some interesting questions. First, the increased electron and ion temperature gradients in the fast ramp case, as well as the separation of about $\delta(r/a) \approx 0.1$ between the electron and ion ITBs [Fig. 7(b)], are maintained only until approximately $t \approx 0.25$ s. At late times, however, the overall T_e , T_i , n_e and rotation profiles become very similar in both discharges. The corresponding transport situation is illustrated in Fig. 10(a), indicating that by $t \approx 0.36$ s, in the fast ramp case the electron and ion barriers have relaxed into a broad region having χ_e and χ_i around a few m^2/s , while in the slow ramp case both χ_e and χ_i decreased inside the region $r/a < 0.7$, to create a transport picture very similar to that in the fast ramp case. The global confinement times are also similar in this regime ($\tau_E \approx 70$ – 75 ms in both discharges at 0.36 s, reaching a global $\tau_E \approx 95$ – 100 ms in the fast ramp

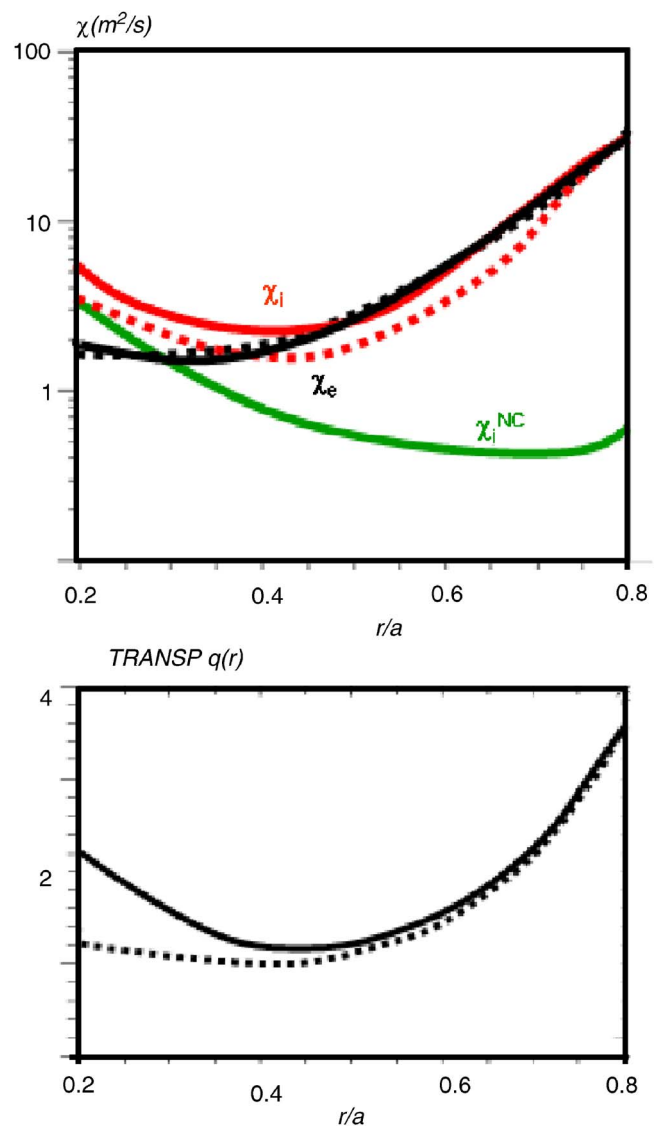


FIG. 10. (a) Electron, ion, and neoclassical diffusivity at $t \approx 0.36$ s in the fast ramp discharge (solid lines) and the slow ramp discharge (dotted lines). The 20 ms variability is small in this case. (b) TRANSP predicted safety factor profiles at the same time point (fast ramp case, solid line; slow ramp, dotted line).

case at $t \approx 0.43$ s, or about 2.5 times the tokamak L-mode scaling).

As concerns the evolution of the q -profiles, TRANSP computes that in the fast ramp shot $q(r)$ remains strongly reversed until late, as shown in Fig. 10(b). (The appearance of 1/1 modes indicates however that q_{\min} is nearer to unity than computed, likely due to the effect of off-axis sawteeth.) The strong reversal can be interpreted as the combined effect of strong current drive and good electron confinement early on in the discharge. Interestingly, TRANSP indicates that at late times the magnetic shear begins to reverse also in the slow ramp case [Fig. 10(b)], where the electron confinement is initially poor. The magnetic diffusion calculation should be more accurate in this case, since the slow ramp plasma does not exhibit any MHD reconnections which could redistribute the current nondiffusively.

The main components of the current profile in the slow

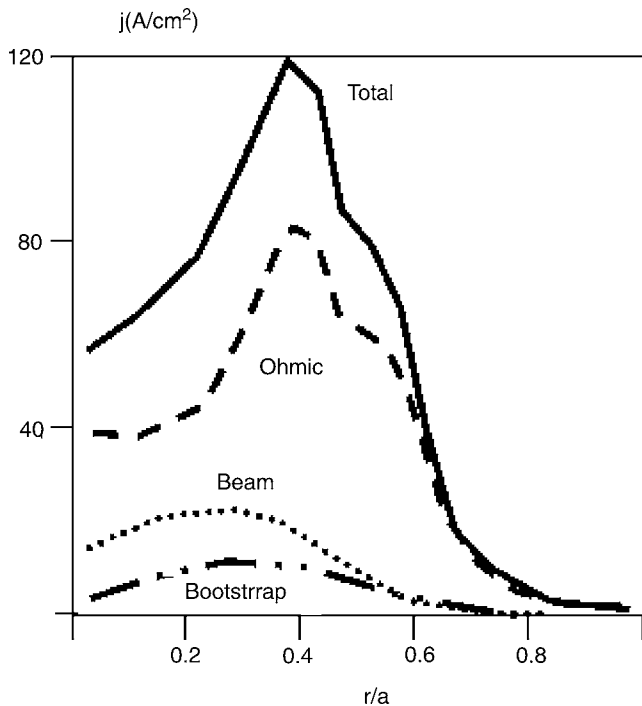


FIG. 11. Main components of the current profile in the slow ramp discharge, at $t=0.36$ s.

ramp case at $t \approx 0.36$ s are shown in Fig. 11. As seen, although the off-axis bootstrap current is increasing with time in these L-modes, the current profile is still largely determined by the ohmic component and by the approximately constant, beam driven component. The characteristic time for the relaxation of the current profile is of the order of 0.2–0.3 s in these plasmas. The “spontaneous” shear reversal in the slow ramp case reflects therefore mainly the slowing down of the ohmic current penetration (current being continuously driven throughout the discharge), due to a steadily increasing core T_e (Fig. 2), correlated with the above discussed decrease in transport. A question here is therefore if the transport decrease in the slow ramp case can also be explained through the buildup of shear reversal, as in a “slow-motion” version of the fast ramp case.

Another question in these experiments is that at $t \geq 0.26$ s in the slow ramp case, the USXR and Thomson scattering data suggest a spontaneous transition to an improved transport situation. The USXR profiles show a slow (≈ 10 ms) “reconnection-like” event, which broadens the emissivity profile bringing it closer to that in the fast ramp case [Fig. 12(a)]. After an initial drop, the Thomson temperature profile also significantly broadens by the end of this evolution [Fig. 12(b)]. Broadening of the C density profile is also shown by the charge exchange recombination spectroscopy data. The slow time scale suggests a transport rather than a MHD effect, possibly indicating a spontaneous transition to improved electron confinement.

The χ_e profiles before ($t \approx 0.243$ s) and after the transition ($t \approx 0.276$ s) are shown in Fig. 13, together with the q -profiles predicted by TRANSP. During this transition the thermal electron transport decreases by 30%–40% outside $r/a \approx 0.4$ and increases by a comparable fraction inside this

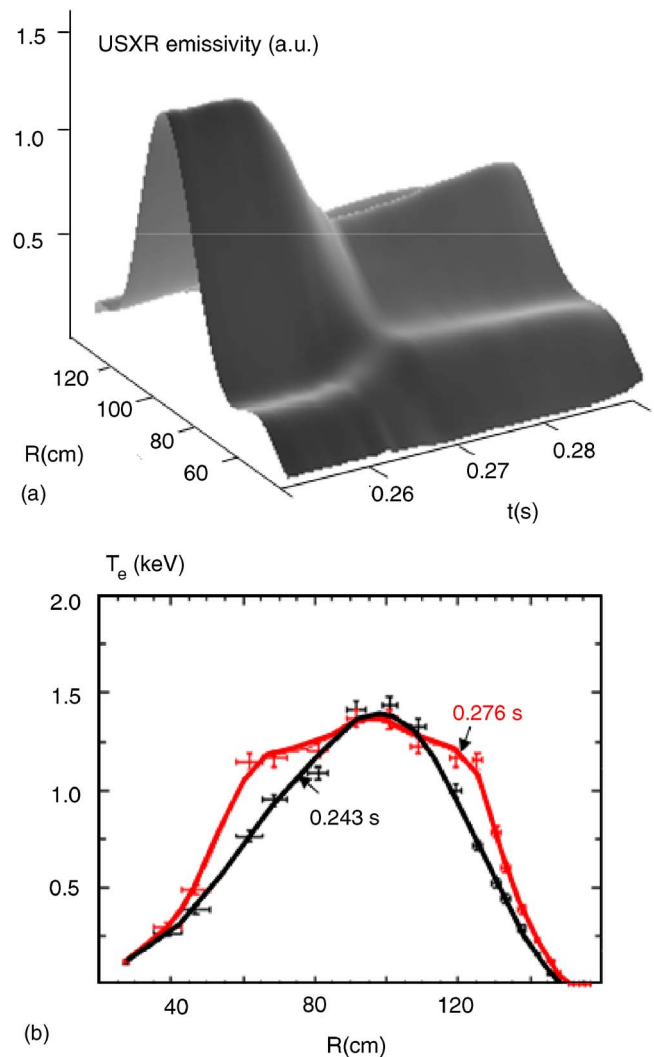


FIG. 12. (a) Evolution of the USXR emissivity during slow, reconnection-like event observed around $t \approx 0.26$ s in the slow ramp discharge. The emissivity reflects the broadening of the electron temperature, density and impurity density. (b) Temperature profiles measured by Thomson scattering before and after the event.

radius. The TRANSP computed q -profile undergoes only a small change. Spontaneous transport transitions when a low order rational- q surface comes into the plasma have been reported from several tokamaks.¹ Interestingly, the transition occurs shortly after the end of the current ramp. Whether there is a more systematic correlation with certain values of the safety factor, or rather with the reduction in the current drive also remains to be investigated.

In addition, it is difficult to explain why at late times in the low density L-modes (Fig. 10), while the electron transport is lower than in the intermediate density L-mode (Fig. 1), the ion transport increases several fold above the neoclassical range. Modeling of the penetration of injected neon as in Ref. 9 indicates also a similar increase in the impurity diffusivity in the low density L-modes. This diverges from the linear microstability assessment, which predicts that for the situation in Fig. 10 the ITG-TEM growth rates are well below the $\mathbf{E} \times \mathbf{B}$ shearing rates throughout most of the plasma.

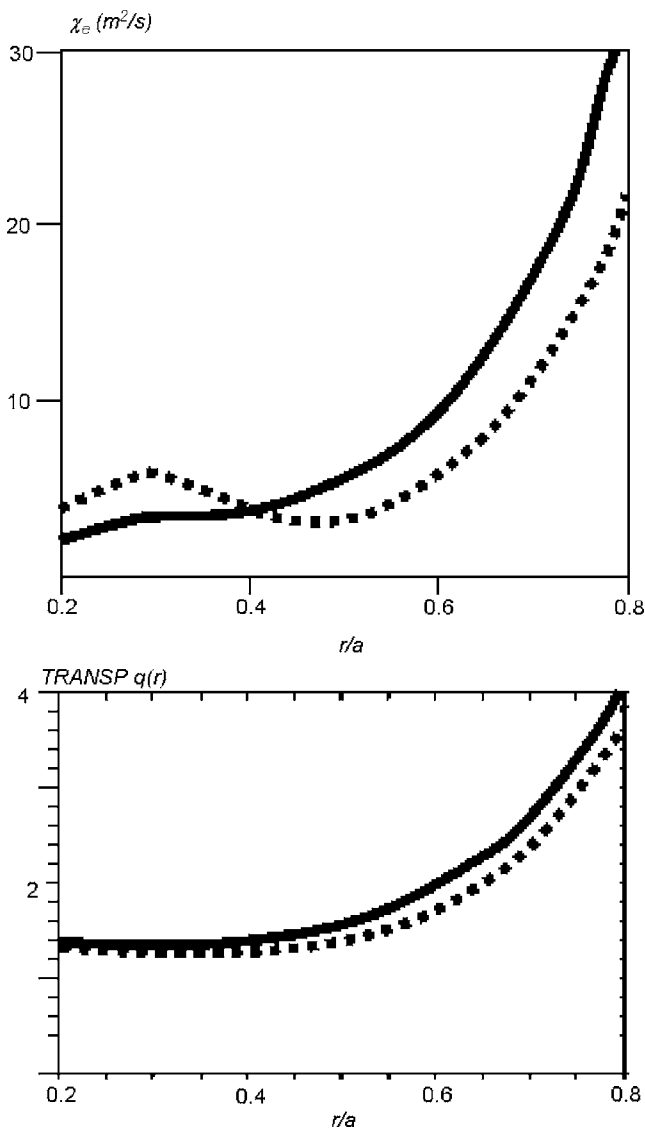


FIG. 13. TRANSP computed χ_e and q -profiles before ($t \approx 0.243$ s, solid lines) and after ($t \approx 0.276$ s, dashed lines) the slow profile change illustrated in Fig. 12.

Finally, in the central region ($r/a \leq 0.25$) of the discharges estimated to have negative shear, the T_e profile is flat, while the T_i profile is either flat or hollow (Fig. 3). Such flat temperature profiles are also observed in large aspect-ratio tokamak plasmas having ITBs with strongly reversed q -profile.¹ While large neoclassical transport at low poloidal field might eventually explain the flat T_i profile, it is not clear what drives rapid electron transport in the absence of measurable gradients. Furthermore, if the hollow T_i profiles are not an experimental artifact, this observation raises anew the possibility of anomalous ion heating in NSTX³¹ or alternately, that of anomalous heat pinches.

VII. CONCLUSIONS

The present experiments were motivated by the question as to whether the current profile can directly influence electron transport on NSTX. To this end, we aimed to produce discharges with different magnetic shears, while having other

parameters potentially important for transport, like $\mathbf{E} \times \mathbf{B}$ shearing rates, T_i/T_e ratio, density profiles, collisionality, and β as much as possible similar. Changing the current ramp-rate and onset of beam heating in low density L-modes has made indeed substantial changes in the NSTX electron and ion transport, as had been also observed in other devices.¹ The analysis of USXR and magnetic fluctuations, together with current diffusion calculations, point to changes in magnetic shear as a primary cause for the transport changes, with strong negative shear being at least a necessary condition for the creation of electron and ion ITBs. Consistent with the experiment, the linear microstability analysis predicts strong suppression of most electron and ion instabilities in conditions of strong negative shear.

More puzzles arise nevertheless from the present experiments. Clearly, measurements of low- and high- k electrostatic and magnetic fluctuations deep in the NSTX core, compared with predictions of nonlinear electromagnetic calculations are needed to assess the possible roles of electrostatic and microtearing modes in the ST transport. Theoretical efforts are underway at both NSTX and MAST,^{13,25,26} while high- and low- k microwave scattering diagnostics are developed at NSTX to detect density fluctuations. The possibility of using the fast capability of the MSE diagnostic for the measurement of core magnetic fluctuations is also being examined.

ACKNOWLEDGMENTS

This work is supported by US DOE grant DE-FG02-99ER54523 at the Johns Hopkins University and by US DOE contract DE-AC02-76CH03073 at PPPL.

- ¹J. W. Connor, T. Fukuda, X. Garbet, C. Gormezano, V. Mukhovatov, M. Wakatani, the ITB Database Group, and the ITPA Topical Group on Transport and Internal Barrier Physics, Nucl. Fusion **44**, R1 (2004).
- ²P. Terry, Rev. Mod. Phys. **72**, 109 (2000).
- ³X. Garbet, P. Mantica, C. Angioni *et al.*, Plasma Phys. Controlled Fusion **46**, B557 (2004).
- ⁴C. Challis, Plasma Phys. Controlled Fusion **46**, B23 (2004).
- ⁵G. Rewoldt, W. M. Tang, S. Kaye, and J. Menard, Phys. Plasmas **3**, 1667 (1996).
- ⁶M. Kotschenreuther, W. Dorland, Q. P. Liu, M. C. Zarnstorff, R. L. Miller, and Y. R. Lin-Liu, Nucl. Fusion **40**, 677 (2000).
- ⁷M. Ono, S. M. Kaye, Y.-K. M. Peng *et al.*, Nucl. Fusion **40**, 557 (2000).
- ⁸B. P. LeBlanc, R. E. Bell, S. M. Kaye *et al.*, Nucl. Fusion **44**, 513 (2004).
- ⁹D. Stutman, M. Finkenthal, R. E. Bell, S. M. Kaye, B. P. LeBlanc, J. E. Menard, E. J. Synakowski, D. S. Darrow, V. Soukhanovskii, C. Bourdelle, and NSTX Team, Phys. Plasmas **10**, 4387 (2003).
- ¹⁰H. Meyer, A. R. Field, R. J. Akers *et al.*, Plasma Phys. Controlled Fusion **46**, A291 (2004).
- ¹¹R. J. Akers, J. W. Ahn, G. Y. Antar *et al.*, Plasma Phys. Controlled Fusion **45**, A175 (2003).
- ¹²S. M. Kaye, M. G. Bell, R. E. Bell *et al.*, Nucl. Fusion **45**, S168 (2005).
- ¹³C. M. Roach, D. J. Applegate, J. W. Connor *et al.*, Plasma Phys. Controlled Fusion **47**, B323 (2005).
- ¹⁴W. A. Houlberg, K. C. Shaing, S. P. Hirshman, and M. C. Zarnstorff, Phys. Plasmas **4**, 3230 (1997).
- ¹⁵D. A. Gates, H. E. Mynick, and R. B. White, Phys. Plasmas **11**, L45 (2004).
- ¹⁶A. R. Field, R. J. Akers, and C. Brickley, in Proceedings of Invited Papers, 20th IAEA Fusion Energy Conference, Vilamoura, 2004, p. EX/P2-11.
- ¹⁷S. S. Medley, N. N. Gorelenkov, R. Andre, R. E. Bell, D. S. Darrow, E. D. Fredrickson, S. M. Kaye, B. P. LeBlanc, A. L. Roquemore, and the NSTX Team, Nucl. Fusion **44**, 1158 (2004).
- ¹⁸M. Tournianski, R. Akers, P. Carolan, and D. Keeling, Plasma Phys. Con-

- trolled Fusion **47**, 671 (2005).
- ¹⁹J. Ongena, M. Evrard, and D. McCune, Trans. Fusion Technol. **33**, 181 (1998).
- ²⁰D. Stutman, M. Finkenthal, H. W. Moos, K. B. Fournier, R. Kaita, D. Johnson, and L. Roquemore, Rev. Sci. Instrum. **74**, 1982 (2003).
- ²¹C. Nardone, Plasma Phys. Controlled Fusion **34**, 1447 (1992).
- ²²T. S. Hahm and K. H. Burrell, Phys. Plasmas **2**, 1648 (1995).
- ²³W. X. Wang, W. M. Tang, F. L. Hinton, L. E. Zakharov, R. B. White, and J. Manickam, Comput. Phys. Commun. **164**, 178 (2004).
- ²⁴M. Kotschenreuther, G. Rewoldt, and W. M. Tang, Comput. Phys. Commun. **88**, 128 (1995).
- ²⁵M. H. Redi, W. Dorland, C. L. Fiore, D. Stutman, S. M. Kaye, J. Menard, and G. Rewoldt, in Proceedings of Invited Papers of 32nd EPS Conference on Plasma Physics, Tarragona, 2005, p. P5.041.
- ²⁶M. H. Redi, S. Kaye, W. Dorland *et al.*, in Proceedings of Invited Papers of 31st EPS Conference on Plasma Physics, London, 2004, p. P2.162.
- ²⁷X. Garbet and R. E. Waltz, Phys. Plasmas **3**, 1898 (1996).
- ²⁸T. S. Hahm, Z. Lin, P. H. Diamond *et al.*, in Proceedings of Invited Papers of 20th IAEA Fusion Energy Conference, Vilamoura, 2004, p. TH/1-4.
- ²⁹A. Thyagaraja, P. J. Knight, M. R. de Baar *et al.*, Phys. Plasmas **12**, 090907 (2005).
- ³⁰R. E. Waltz, J. M. Candy, and M. N. Rosenbluth, Phys. Plasmas **9**, 1938 (2002).
- ³¹D. A. Gates and NSTX National Research Team, Phys. Plasmas **10**, 1659 (2003).